Velocimetry of cold atoms by matter-wave interferometry

Max Carey,* Jack Saywell, Mohammad Belal, and Tim Freegarde
School of Physics & Astronomy, University of Southampton, Highfield, Southampton SO17 1BJ, United Kingdom

(Received 12 February 2018; published 28 February 2019; corrected 17 September 2020)

We present an elegant application of matter-wave interferometry to the velocimetry of cold atoms whereby, in analogy to Fourier transform spectroscopy, the one-dimensional velocity distribution is manifest in the frequency domain of the interferometer output. By using stimulated Raman transitions between hyperfine ground states to perform a three-pulse interferometer sequence, we have measured the velocity distributions of clouds of freely expanding ^{85}Rb atoms with temperatures of 34 and 18 μK. Quadrature measurement of the interferometer output as a function of the temporal asymmetry yields velocity distributions with excellent fidelity. Our technique, which is particularly suited to ultracold samples, compares favorably with conventional Doppler and time-of-flight techniques, and it reveals artefacts in standard Raman Doppler methods. The technique is related to, and provides a conceptual foundation of, interferometric matter-wave accelerometry, gravimetry, and rotation sensing.

DOI: 10.1103/PhysRevA.99.023631

I. INTRODUCTION

In the macroscopic world, we measure an object's temperature by bringing it into thermal equilibrium with a small probe. When the object is a cloud of cold atoms, the tiny thermal mass requires a thermodynamic probe on the atomic scale [1]; and inhomogeneous cooling, incomplete thermalization, coupling to electronic energy levels, and nonequilibrium quantum thermodynamics can mean that the temperature is poorly defined [2]. It is therefore common to characterize a cold-atom sample by its velocity distribution, from which the kinetic temperature may be found by subsequent parametrization.

Popular methods of measuring velocity distributions, such as time-of-flight imaging [3], Raman [4,5], and Bragg [6,7] Doppler spectroscopy rely upon separate interactions with small slices of the velocity distribution to build up a complete measurement. Each involves the signal from only a small number of atoms, and there are artefacts from the initial cloud size and measurement-induced perturbation of the velocity distribution. Despite a variety of enhancements [8–10], precise interpretation of the results requires care [5,11].

Here we present an alternative method of cold-atom velocimetry by matter-wave interferometry, in which broadband interactions with laser pulses allow all the atoms within the cloud to be interrogated simultaneously, permitting a significant improvement in the measurement signal-to-noise ratio while subjecting the sample to only the smallest perturbations and constraints. In contrast to Doppler spectroscopy, the technique is particularly suited to the lowest temperatures. While it can be considered a method of measuring the temperature-dependent coherence length of the atomic wave packet [12–14], we show here that it allows the velocity distribution to be measured in detail. It provides an elegant conceptual underpinning of matter-wave accelerometry, gravimetry, and rotation sensing, in which differential velocity measurements are performed by two sequences in succession [15–19], and as a result inspires adaptations that, for example, offer immunity to mechanically induced laser phase noise between the two measurements [20].

II. CONCEPTUAL OVERVIEW

Matter-wave interferometry is performed by sequences of pulsed interactions, resonant with the two-state quantum system ($|1\rangle$, $|2\rangle$), that are separated by periods of free evolution [21]. Prior to each sequence, the atoms are pumped into one of the two states, $|1\rangle$. The first pulse then places the atom into a quantum superposition of the two states, whose phase is determined by that of the interaction field. The effect of subsequent pulses then depends upon the phase difference accrued between the time base of the interaction field and the atomic state [17].

An example is the Ramsey interferometer [22], consisting of two pulses separated by a free-evolution period τ as depicted in Fig. 1(a). Each "$\pi/2$-pulse" lasts a quarter of the Rabi oscillation period, and thus converts either of the two atomic states into an equal superposition. In the case in which $\tau = 0$, the two pulses combine to form a "π-pulse," which transfers atoms from one state to the other.

For $\tau > 0$, the first pulse leaves each atom in a superposition which then evolves freely to accrue a relative phase Φ according to the atoms' environment and trajectory. The phase determines the effect of the second pulse of the sequence, and it can thus be measured by monitoring the atomic state populations once the sequence is complete.

If the interaction is with a pulsed laser beam, then atoms propagating with velocity v_z along the beam axis will experience a Doppler-shifted field, which gives the superposition phase Φ a dependence on the distance traveled during the evolution time τ. If there are no other phase contributions, then

$$\Phi = \mathbf{k} \cdot \mathbf{v}\tau = k v_z \tau, \tag{1}$$

*max.carey@soton.ac.uk

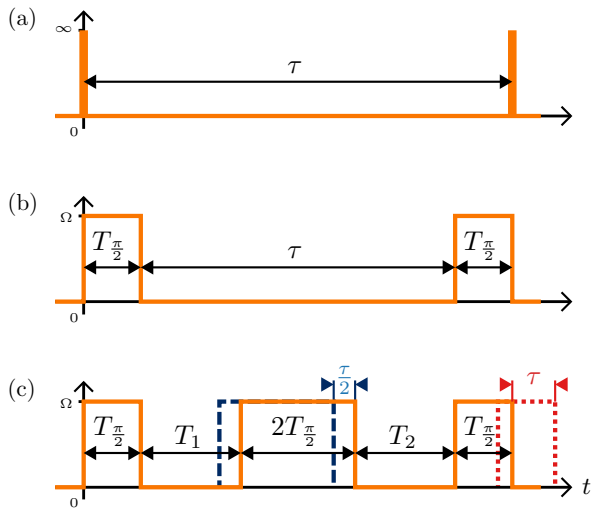

FIG. 1. Temporal pulse profiles for the interferometer sequences considered here. (a) Ramsey sequence with ideal, zero-length, pulses. (b) Ramsey sequence with realistic, finite-length, pulses. (c) Asymmetric Mach-Zehnder sequence with realistic pulses.

where k is the laser wave number [23,24]. The second pulse maps this phase onto atomic state probabilities so that, with ideal pulses that perform this mapping exactly, the probability that a given atom is in the second atomic state $|2\rangle$ is

$$|c_2|^2 = \tfrac{1}{2}[1 + \cos(kv_z\tau)], \tag{2}$$

and thus the fraction of a statistical ensemble in state $|2\rangle$ will be

$$\mathcal{S}(\tau) = \int_{-\infty}^{\infty} P(v_z)\frac{1}{2}[1 + \cos(kv_z\tau)]dv_z, \tag{3}$$

where $P(v_z)$ is the normalized distribution of velocity components v_z in the beam direction. Each velocity class v_z hence contributes to the interferometer signal a component that varies sinusoidally with τ, with frequency kv_z and amplitude proportional to $P(v_z)$, akin to the contributions from different wavelengths of light to the signal produced when varying the arm length of a Michelson interferometer in Fourier transform spectroscopy [25,26]. The velocity distribution is thus mapped onto the frequency domain of the signal, but, due to the symmetry of the cosine function, positive and negative velocities cannot be distinguished.

If the laser phase is advanced by ϕ between the two interferometer pulses, this phase is mapped onto the output signal such that

$$\mathcal{S}(\phi, \tau) = \int_{-\infty}^{\infty} P(v_z)\frac{1}{2}[1 + \cos(kv_z\tau - \phi)]dv_z. \tag{4}$$

The absolute value of the Fourier transform of the quantity

$$\mathcal{S}_I + i\mathcal{S}_Q \equiv \mathcal{S}(0, \tau) + i\mathcal{S}(\pi/2, \tau) \tag{5}$$

is then proportional to the velocity distribution $P(kv_z)$, expressed as a function of the frequency kv_z [27,28].

III. A MACH-ZEHNDER INTERFEROMETER FOR ATOM VELOCIMETRY

The astute reader will notice that the Fourier transform of the signal defined in Eq. (5) can only be measured experimentally for positive pulse separations τ, and that the signal is thus effectively multiplied by a Heaviside step function. With ideal interferometer pulses that perform perfect, instantaneous operations upon all atoms [Fig. 1(a)], this would introduce an orthogonal component to the Fourier transform that could be separated from the velocity information, but in practice deconvolution becomes intractable because pulses of finite duration [Fig. 1(b)] themselves exhibit Doppler sensitivity, introducing a velocity-dependent amplitude and phase shift that we have explored in more detail in [27].

In this work, we therefore interleave a "mirror" π-pulse between the "beam-splitters" of our interferometer, as shown in Fig. 1(c). In its time-symmetrical form ($T_2 = T_1$), atoms divide their time equally between the two interferometer states, and the interferometer forms a basic "composite pulse" [29] in which systematic contributions to the phase accrued during the first evolution period T_1 are reversed during the second period T_2. This Mach-Zehnder arrangement forms the basis for atom interferometric inertial sensing, since steady velocity-dependent phase shifts cancel and only the phase shifts due to changes in velocity remain [15–19].

When the interferometer is asymmetric, however, we retain the velocity sensitivity according to the temporal asymmetry $\tau = T_2 - T_1$, which can be varied continuously over both negative and positive values, while taking advantage of partial cancellation of phase shifts accrued during the pulses themselves [30].

To maintain a constant atom cloud expansion in our experiments, we set the total interferometer duration $T = T_1 + T_2$ to a constant and vary τ between $-T$ and T. We show in Appendix A that some Doppler sensitivity remains in a velocity-dependent modification of the fringe amplitude that could be corrected for in subsequent analysis, and the introduction of subharmonics with twice the fringe period that enhance the apparent probability of lower atomic velocities. Provided the Doppler shift is no more that 0.4 of the Rabi frequency, however, these effects are negligible.

IV. EXPERIMENTAL PROCEDURE

Our experimental apparatus [29,31] is shown schematically in Fig. 2. A 3D magneto-optical trap (MOT) of ^{85}Rb atoms is formed using a cooling laser detuned by the order of the natural linewidth to the red of the $|5S_{1/2}, F = 3\rangle \rightarrow |5P_{3/2}, F' = 4\rangle$ cycling transition, and a repump laser locked to the $|5S_{1/2}, F = 2\rangle \rightarrow |5P_{3/2}, F' = 3\rangle$ transition ensures that atoms are not lost from the cooling cycle to the $|5P_{3/2}, F' = 3\rangle$ state. After a 1 s loading time, the magnetic field gradient is extinguished and the cooling laser reduced in power, leaving the atoms to undergo sub-Doppler cooling in an optical molasses. After a further period of typically 11 ms, the repump laser is extinguished and the cooling beam optically pumps the atoms into the $|5S_{1/2}, F = 2\rangle$ state for ~4 ms with a $1/e$ time constant on the order of 100 μs [32].

The power levels and timescales are varied in order to achieve different sample temperatures, but the time between magnetic field extinction and the interferometry sequence is always kept to 15 ms in order to ensure that the magnetic field, which continues to vary slightly through eddy effects, is correctly nulled at the time of the interferometer sequence by additional shim coils such that the magnetic sublevels are degenerate to within $<2\pi \times 50$ kHz.

Our interferometry is conducted with two-photon Raman transitions between the $|5S_{1/2}, F = 2\rangle$ and $|5S_{1/2}, F = 3\rangle$ hyperfine ground states, which have a frequency splitting of $\omega_0 = 2\pi \times 3.036$ GHz. Two counterpropagating laser beams, differing in frequency by $\omega_0 + \delta_{\text{laser}}$, where δ_{laser} is a variable detuning, are detuned from the $|5S_{1/2}, F = 3\rangle \rightarrow |5P_{3/2}, F' = 4\rangle$ transition by $\Delta_{\text{1-photon}} \approx 2\pi \times 5$ GHz. This allows long-lived ground states to be used, while the Doppler sensitivity is characterized by an effective wave number $k_{\text{eff}} = 2\pi/\lambda_{\text{eff}}$, with $\lambda_{\text{eff}} \approx (780/2)$ nm.

These beams are derived from an amplified free-running distributed feedback (DFB) laser (Eagleyard EYP-DFB-0780-00080-1500-BFW01-0005), with the higher frequency beam formed by the first upper diffracted order from a 310 MHz acousto-optic modulator (AOM) and the lower frequency shift achieved with a 2.7 GHz electro-optic modulator (EOM), from which the carrier frequency is suppressed by a fiber Mach-Zehnder interferometer [33]. The high-frequency EOM sideband remains and, while playing no part in the Raman transition, contributes to the ac Stark shift.

The beams are separately amplified with tapered amplifier diodes, combined on a further AOM for fast (∼50 ns) shuttering, and then separated again by polarization in order to be coupled into separate fibers, which transfer the light to the MOT chamber. At the fiber outputs the beams are orthogonally, linearly, polarized and pass through Topag GTH-4-2.2 refractive beam shapers, which give them a 1.4 mm square profile with ∼15% intensity variations across the MOT cloud at the focus of 750 mm focal length lenses. This allows for an intensity around 5 W cm^{-2} per frequency component over the interferometry region.

The interferometer read-out is performed by illuminating the atoms with the MOT cooling light for 300 μs and collecting the fluorescence onto a Hamamatsu H7422-50 photomultiplier tube (PMT). The atoms are then pumped back into the $|5S_{1/2}, F = 3\rangle$ for ∼50 μs by the resonant repump light [32], and then reilluminated by the cooling light for a further 300 μs. Exponential decay functions are fitted to the cooling fluorescence PMT signals, and the ratio of their amplitudes is used as a measure of the fraction of atoms transferred to the $|5S_{1/2}, F = 3\rangle$ state during the interferometer. Full details and characterization of the read-out process can be found in [34].

The ac Stark shift is determined by measuring the population transfer of a π-pulse measured as a function of the Raman detuning δ_{laser} before interferometry. The detuning is then set to coincide with the peak transfer. This detuning introduces a shift in the frequency domain of the signal, which should be subtracted from the derived velocity distribution in order to extract a representative result. When this shift is greater than the width of the Doppler profile, the dc component of the signal does not coincide with any atomic velocity so that there is no ambiguity in analysis.

V. RESULTS

Figure 3 shows typical output from the interferometer, with a detuning $\delta_{\text{laser}} = -2\pi \times 1050$ kHz introduced from the two-photon Raman resonance to offset the ac Stark shift during the pulses. The in-phase and quadrature fringes correspond to $-\mathcal{S}_I$ and $\mathcal{S}_Q$ from Equation (5), with the inversion of the in-phase component arising from the additional rotation by π. The fast Fourier transform (FFT) of these data gives the velocity distribution, without need for further determination of fringe visibility, and is shown, in units of velocity, in Fig. 4.

The velocity resolution of the FFT is determined by the range of τ, limited in principle to the time it takes atoms to leave the interaction region. Our data, in the range $|\tau| < 10\ \mu$s (spanning $\Delta\tau = 20\ \mu$s), give a velocity resolution of $\delta v = 1/(k_{\text{eff}}\Delta\tau) \approx 20$ mm s^{-1}. The value $\delta\tau$ by which τ is incremented between adjacent data points, in this case $\delta\tau = 50$ ns,

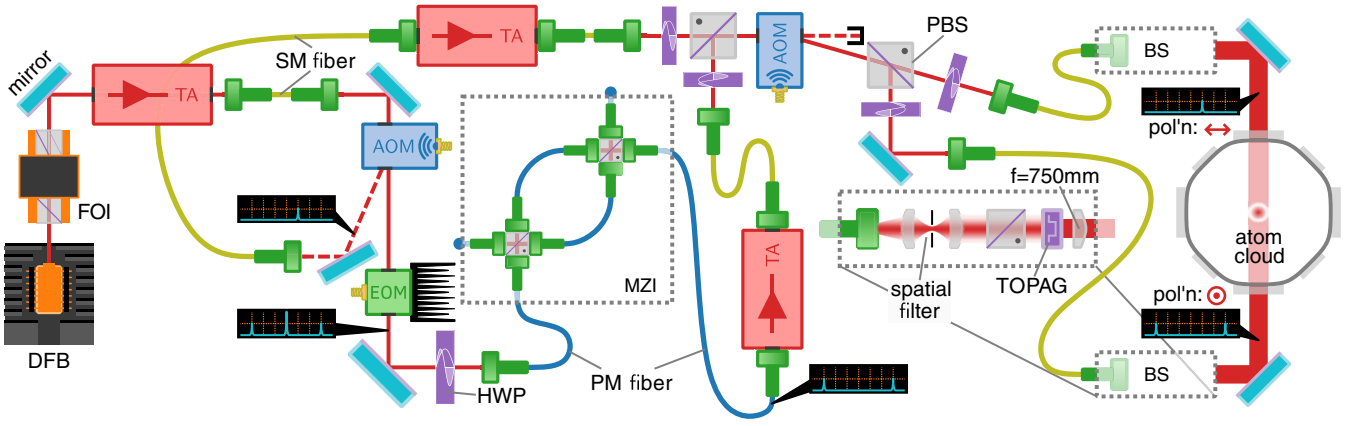

FIG. 2. Schematic for Raman interferometer: Distributed feedback laser diode (DFB), Faraday optical isolator (FOI), tapered amplifier (TA), acousto-optic modulator (AOM), electro-optic modulator (EOM), half-wave-plate (HWP), polarizing beam-splitter (PBS), Topag GTH-4-2.2 refractive beam-shaper (TOPAG), beam-shaping optics (BS), single-mode (SM) and polarization-maintaining (PM) fibers, fiber Mach-Zehnder filter (MZI). MOT optics are not shown, and only one instance is labeled for some repeated symbols.

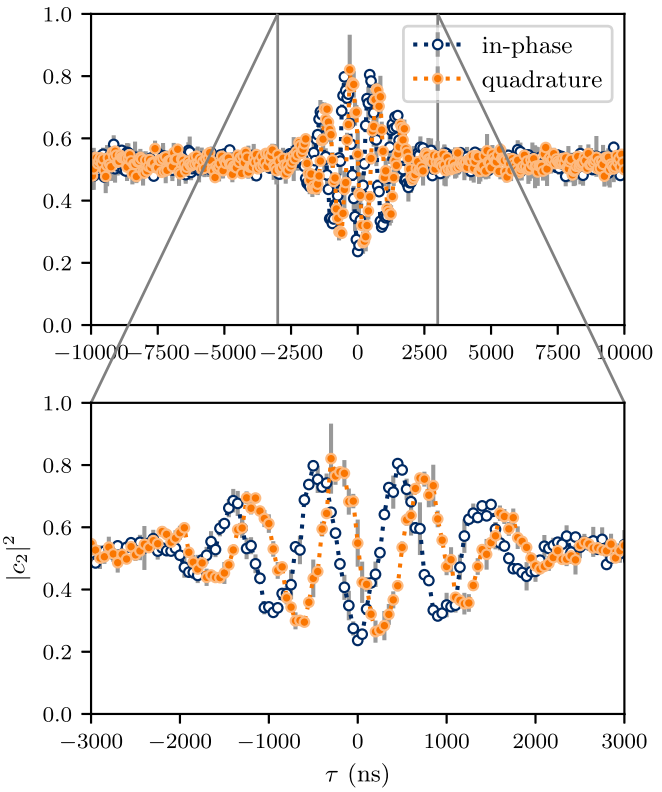

FIG. 3. Measurements of fractional population transfer $|c_2|^2$ as a function of temporal asymmetry τ for interferometers with (filled orange circles) and without (open blue circles) a $\pi/2$ phase shift before the final recombination pulse. Each point is an average of two measurements, with gray error bars representing the standard deviation. A detuning of $\delta_{\text{laser}} = -2\pi \times 1050$ kHz from the hyperfine splitting results in oscillations that appear within an envelope whose shape is governed by the velocity distribution.

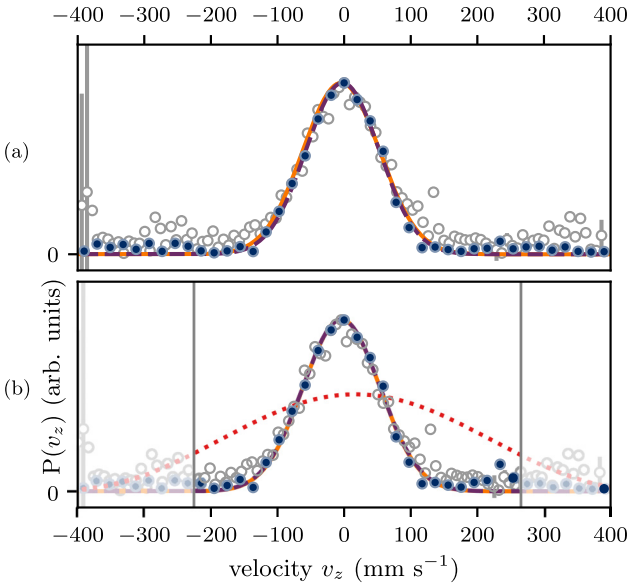

FIG. 5. Absolute value of the FFT of data in Fig. 3, filled (blue) circles, overlaid upon a velocity profile determined by Raman Doppler spectroscopy, empty (gray) circles, in units of velocity. Solid (orange) lines are a Gaussian fit to the spectroscopic data, with a temperature of 33.6 ± 1.5 μK, and dashed (purple) lines show Gaussian fits to the interferometric data. Plot (a) uses raw FFT data, and the Gaussian fit is narrower than the spectroscopic measurement with a temperature of 31.0 ± 1.5 μK. Plot (b) has a correction factor applied, multiplying each point by the reciprocal of the theoretical amplitude $\mathcal{A}(k_{\text{eff}}v_z)$ based on our experimental parameters, overlaid as a dashed (red) line. Only points in the $\mathcal{A} > 0.4$ range (highlighted) were corrected to avoid amplifying noise at the extremities, bringing the fitted temperature to 34.1 ± 1.6 μK in agreement with the fit to the spectroscopic data. The ac Stark shift-induced offset from the spectroscopic data has been subtracted, centering it on the interferometric data at $v_z = -4.5$ mm s^{-1} to better compare their shapes.

determines the range of velocities that can be measured $\Delta v = 1/(k_{\text{eff}}\delta t)$, although oversampling reduces the sensitivity of the measurement to the noise on any individual data point.

The absolute values of the FFT data [28] are reproduced with the two-photon detuning subtracted in Fig. 5(a), where they are overlaid upon a measurement made by conventional Raman Doppler spectroscopy. Fitted Gaussian profiles, with temperatures of 31.0 ± 1.5 and 33.6 ± 1.5 μK respectively, are shown.

The FFT profile, shown in Fig. 5(a), requires a small correction to account for a slight dependence of the fringe amplitude $\mathcal{A}(k_{\text{eff}}v_z)$ upon atomic velocity. Figure 5(b) shows this velocity dependence (dotted line), together with the corrected velocity distribution which yields the same temperature as the Doppler measurements, with notably enhanced signal-to-noise ratio. This velocity dependence, together with some parasitic contributions to the interferometer output at large detunings, are discussed in Appendix A, and impose an effective upper limit on the range of velocities that can be measured. As these effects depend on the Rabi frequency

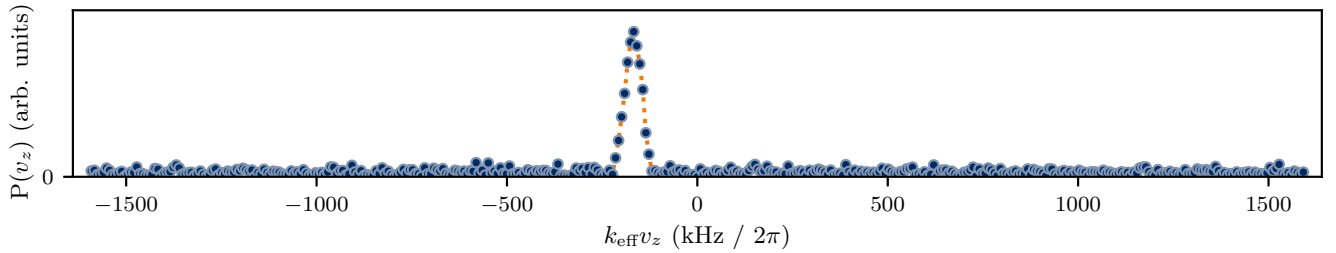

FIG. 4. Absolute value of raw FFT of data in Fig. 3 after baseline subtraction, prior to subtracting the $\delta_{\text{laser}} = -2\pi \times 1050$ kHz laser detuning from the hyperfine splitting, which manifests as a -410 mm s^{-1} shift to the center of the velocity distribution. The quadrature measurement is able to resolve the sign of the displacement, so there is no component with an opposite shift.

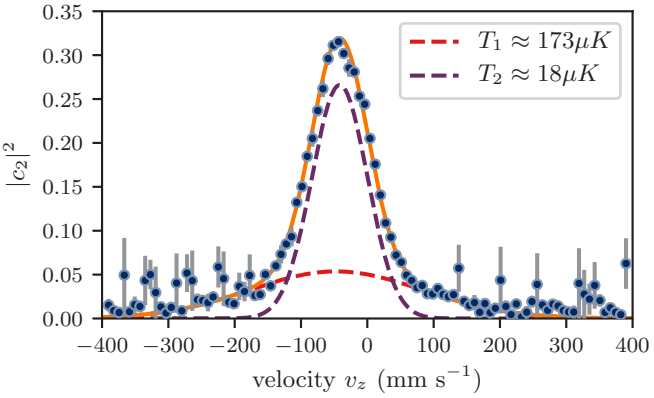

FIG. 6. Doppler spectroscopy velocity profile taken with Raman π-pulses with a single-photon detuning $\sim 2\pi \times 7$ GHz and a Rabi frequency $\Omega_R \approx 2\pi \times 50$ kHz. A single Gaussian does not make a good fit, but a two Gaussian distribution fits well. The solid (orange) line is the sum of the two dashed Gaussians, a cold central peak, and a broader background, which we have previously attributed to inhomogeneous sub-Doppler cooling. The resonance is ac Stark shifted, resulting in the large offset of the distribution from $v_z = 0$.

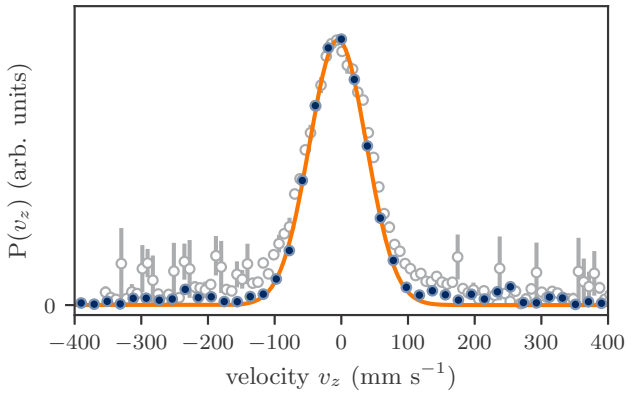

FIG. 7. Interferometric velocimetry measurement, filled circles (blue), overlaid upon the Doppler spectroscopy profile from Fig. 6, empty circles (gray). The measurements were taken under the same conditions, with the offset subtracted from the spectroscopic data to center them on the interferometric profile at $v_z = -5.1$ mm s^{-1}. The solid (orange) line shows a Gaussian fit to the interferometric data, with a temperature of 18.7 ± 0.6 μK corresponding closely to the 17.8 ± 0.9 μK colder Gaussian fitted in Fig. 6. The signal-to-noise ratio of the interferometric measurement is good, and does not show signs of the broad background evident in the spectroscopic measurement.

Ω_R, higher intensity Raman beams could be used to extend this limit. The profile in this instance is slightly displaced to account for a difference of $2\pi \times 40$ kHz between the assumed laser detuning δ_{laser} and the ac Stark shift recorded for this experiment.

The Gaussian fit to the corrected data is centered at $v_z = -4.5 \pm 1.3$ mm s^{-1}. This is in agreement with a second measurement, shown in Fig. 7, centered at $v_z = -5.1 \pm 0.7$ mm s^{-1}. We note that the two-photon recoil velocity for ^{85}Rb is 12 mm s^{-1}; and there could be an impulse imparted to the cloud as the magnetic field is terminated.

VI. DISCUSSION

The velocity distribution determined from our interferometric measurements agrees well for a warm sample with that obtained by conventional Doppler spectroscopy using low-power Raman pulses (single-photon detuning $\sim 2\pi \times 15$ GHz, Rabi frequency $\Omega_R \approx 2\pi \times 25$ kHz). Whereas the interferometric measurements are well represented by a single Gaussian, the Doppler measurements show an additional, broader, component. This is particularly noticeable when a cooler sample, such as that shown in Fig. 6, is probed with a strong Raman field (single-photon detuning $\sim 2\pi \times 7$ GHz, Rabi frequency $\Omega_R \approx 2\pi \times 50$ kHz), yielding a central Gaussian distribution with a temperature of 17.8 ± 0.9 μK superimposed upon a much broader background.

Interferometric measurement under the same conditions, shown in Fig. 7, does not display this broad component, but modeling suggests that this is not a limitation of the interferometric technique. We have previously attributed the broad background to inhomogeneous sub-Doppler cooling [35]; such a distribution might also result if the Doppler technique detected warmer, untrapped atoms outside the region interrogated by the interferometer. The dependence upon the strength of the probe laser in the Doppler measurements, however, suggests that the broadening is an artefact of conventional Doppler methods, perhaps due to off-resonant excitation [5]. This is consistent with several determinations of the atom cloud temperature from measurements of the coherence length of the atomic wave packet by measuring the fringe contrast as a function of wave-packet separation, in each case yielding a temperature below that estimated by Doppler [36] or time-of-flight [12–14] methods.

Time-of-flight measurements are often used for colder samples and condensates [37], but these are limited by the physical extent of the cloud and the imaging resolution [11]. In practice, this means that the time of expansion required to measure the coldest distributions is typically $\sim$10 ms, limiting its usefulness when studying dynamic behavior such as in [38]. Both interferometric and Doppler measurements can be performed faster; such measurements with a Fourier transform limited resolution equivalent to Fig. 7 for a 10 nK cloud could be made in as little as 500 μs. However, the Doppler measurement requires a continuous interaction for this time, increasing the probability of the artefacts we have observed while limiting the resonance to a small number of atoms and reducing the signal-to-noise ratio.

Interferometric measurement, in contrast, ideally involves interactions that last for a small fraction of the total measurement time and interact uniformly with the entire velocity and spatial distribution of the atom cloud so that, on average, half of the atoms contribute to the signal, limited by the finite range that can be addressed in practice. Interferometric velocimetry is hence a particularly effective complement to existing methods and is particularly suitable for colder atom samples in which artefacts such as off-resonant excitation, saturation, and scattering force heating would otherwise distort the measured velocity distributions. It uses techniques, apparatus, and in some cases [7,12] datasets that are often already on hand.

VII. CONCLUSION

We have described the use of Ramsey matter-wave interferometry for the measurement of the velocity distribution, and hence translational temperature, of ultracold rubidium atoms. By using an asymmetrical three-pulse arrangement with switchable pulse phases, we record quadrature signals over both positive and negative effective interferometer durations. The Fourier transform, with correction for the residual Doppler effect within the interferometer pulses themselves, then reveals the atomic velocity distributions with good fidelity because the whole atomic sample contributes to each data point. The technique can distinguish between positive and negative velocities with a quadrature measurement, and is more effective at lower cloud temperatures. It is in many ways complementary to conventional techniques of Doppler-sensitive spectroscopy and time-of-flight measurement, as it is not limited by off-resonant excitation [5] or the physical extent of the atom cloud and measurement beam [11].

The data presented in this paper are available in Ref. [42].

ACKNOWLEDGMENTS

This work was supported by the EPSRC through the UK Quantum Technology Hub for Sensors & Metrology under Grant No. EP/M013294/1, and by Dstl under Contracts No. DSTLX-1000091758 and No. DSTLX-1000097855. The authors are grateful to David Elcock for his contributions to the stabilization and characterization of the optical and RF apparatus.

APPENDIX A: ANALYTICAL MODEL FOR INTERFEROMETER OUTPUT

Here we derive analytical expressions for the output of a Mach-Zehnder atom interferometer, with a temporal asymmetry τ between the two periods of free evolution. We consider two ways of introducing this asymmetry:

(a) Keeping the total interferometer time constant such that $T_1 = T - \tau/2$ and $T_2 = T + \tau/2$, illustrated by the dashed (blue) line in Fig. 1(c).

(b) Keeping one separation constant such that $T_1 = T$ and $T_2 = T + \tau$, illustrated by the dotted (red) line in Fig. 1(c).

We model the effect of these sequences on a two-level atom with state amplitudes c_1 and c_2, assuming completely coherent evolution and treating pulses in the rotating-wave approximation [39].

Between the pulses, the superposition accrues phase at a rate equal to the atom-laser detuning $\Delta = \delta_{\text{laser}} + \delta_{\text{Doppler}}$, in which we include the laser detuning from the state splitting δ_{laser} in addition to the velocity-dependent detuning $\delta_{\text{Doppler}} = kv_z$. Free evolution for a period T can then be represented by the matrix

$$\mathbf{U}(T) = \begin{pmatrix} e^{-i\Delta\cdot T/2} & 0 \\ 0 & e^{i\Delta\cdot T/2} \end{pmatrix}, \tag{A1}$$

acting on a state vector $\binom{c_1}{c_2}$.

During the pulses, the superposition undergoes a rotation in Hilbert space [40] whose rate and orientation are determined by the on-resonance Rabi frequency Ω and the detuning $\Delta_{\text{ac}} = \Delta - \delta_{\text{ac}}$, which differs from the interpulse detuning by a term δ_{ac} due to the ac Stark shift.

The effect of a pulse of duration T can be solved analytically and, following the formalism of Stoner *et al.* [41], can be represented by the matrix

$$\mathbf{\Omega}(T, \phi_L) = \begin{pmatrix} C(T) & -iS(T, \phi_L) \\ -iS^*(T, \phi_L) & C^*(T) \end{pmatrix} \tag{A2}$$

to act on a state vector, with

$$C(T) = \cos\left(\frac{T}{2}\sqrt{\Delta_{\text{ac}}^2 + \Omega^2}\right) + i\frac{\Delta_{\text{ac}}}{\sqrt{\Delta_{\text{ac}}^2 + \Omega^2}}\sin\left(\frac{T}{2}\sqrt{\Delta_{\text{ac}}^2 + \Omega^2}\right), \tag{A3a}$$

$$S(T, \phi_L) = \frac{\Omega e^{i\phi_L}}{\sqrt{\Delta_{\text{ac}}^2 + \Omega^2}}\sin\left(\frac{T}{2}\sqrt{\Delta_{\text{ac}}^2 + \Omega^2}\right). \tag{A3b}$$

Here we have included an explicit dependence on the laser phase ϕ_L.

After a pure state ($c_1 = 1$, $c_2 = 0$) has been subjected to an interferometer sequence, the excited-state probability $|c_2|^2$ can then be calculated with matrix multiplication. We denote the nth pulse with subscripts $\mathbf{\Omega}_n$, C_n, S_n, etc. so that the output of a three-pulse interferometer with pulse separations $T_{1,2}$ is

$$\begin{aligned} |c_2|^2 &= \left|\begin{pmatrix} 0 & 0 \\ 0 & 1 \end{pmatrix}\mathbf{\Omega}_3\mathbf{U}(T_2)\mathbf{\Omega}_2\mathbf{U}(T_1)\mathbf{\Omega}_1\begin{pmatrix} 1 \\ 0 \end{pmatrix}\right|^2, \\ &= |S_1|^2|S_2|^2|S_3|^2 + |C_1|^2|S_2|^2|C_3|^2 \\ &\quad - 2\,\mathrm{Re}[e^{i\Delta(T_2-T_1)}C_1S_1(S_2^*)^2C_3^*S_3] \\ &\quad + |S_1|^2|C_2|^2|C_3|^2 + |C_1|^2|C_2|^2|S_3|^2 \\ &\quad + 2\,\mathrm{Re}[e^{i\Delta(T_1+T_2)}C_1^*S_1^*(C_2^*)^2C_3^*S_3] \\ &\quad + 2(|C_3|^2 - |S_3|^2)\,\mathrm{Re}[e^{-i\Delta\cdot T_1}C_1S_1C_2S_2^*] \\ &\quad + 2(|C_1|^2 - |S_1|^2)\,\mathrm{Re}[e^{i\Delta\cdot T_2}C_2^*S_2^*C_3^*S_3]. \end{aligned} \tag{A4}$$

To proceed we note that, for the Mach-Zehnder interferometers under consideration,

$$C_3 = C_1, \tag{A5a}$$

$$S_3 = e^{i\phi}S_1, \tag{A5b}$$

$$\arg(S_1) = \arg(S_2) \Rightarrow S_1^*S_2 = S_1S_2^* = |S_1||S_2|, \tag{A5c}$$

where ϕ is an advance in the laser phase introduced prior to the final pulse. This allows us to write Eq. (A4) as

$$\begin{aligned} |c_2|^2 &= |S_1|^4|S_2|^2 + |C_1|^4|S_2|^2 + 2|S_1|^2|C_2|^2|C_1|^2 \\ &\quad - 2|C_1|^2|S_1|^2|S_2|^2\cos[\Delta(T_2 - T_1) + \phi] \\ &\quad + 2|S_1|^2\,\mathrm{Re}\left[C_1^2C_2^2\right]\cos[\Delta(T_1 + T_2) + \phi] \\ &\quad + 2|S_1|^2\,\mathrm{Im}\left[C_1^2C_2^2\right]\sin[\Delta(T_1 + T_2) + \phi] \\ &\quad + 2(|C_1|^2 - |S_1|^2)|S_1||S_2|\,\mathrm{Re}[C_1C_2] \\ &\quad \times [\cos(\Delta\cdot T_1) + \cos(\Delta\cdot T_2 + \phi)] \\ &\quad + 2(|C_1|^2 - |S_1|^2)|S_1||S_2|\,\mathrm{Im}[C_1C_2] \\ &\quad \times [\sin(\Delta\cdot T_1) + \sin(\Delta\cdot T_2 + \phi)]. \end{aligned} \tag{A6}$$

Let us first consider case (a), the interferometer keeping the free-evolution time constant, such that $T_{1,2} = T \mp \tau/2$. Noting that

$$\sin\left[\Delta\left(\frac{\tau}{2}+T\right)+\phi\right]+\sin\left[\Delta\left(T-\frac{\tau}{2}\right)\right] = 2\sin\left(\Delta\cdot T+\frac{\phi}{2}\right)\cos\left(\Delta\frac{\tau}{2}+\frac{\phi}{2}\right), \tag{A7a}$$

$$\cos\left[\Delta\left(\frac{\tau}{2}+T\right)+\phi\right]+\cos\left[\Delta\left(T-\frac{\tau}{2}\right)\right] = 2\cos\left(\Delta\cdot T+\frac{\phi}{2}\right)\cos\left(\Delta\frac{\tau}{2}+\frac{\phi}{2}\right), \tag{A7b}$$

the output can be shown to be

$$|c_2|^2 = \frac{1}{2}\left\{\mathcal{C}-\mathcal{A}\cos(\Delta\tau+\phi) + \mathcal{B}\cos\left[\frac{1}{2}(\Delta\tau+\phi)\right]\right\}, \tag{A8}$$

with

$$\mathcal{A} = 4|C_1|^2|S_1|^2|S_2|^2, \tag{A9a}$$

$$\mathcal{B} = 8(|C_1|^2-|S_1|^2)|S_1||S_2| \times[\mathrm{Re}(C_1C_2)\cos(\Delta\cdot T+\phi/2) + \mathrm{Im}(C_1C_2)\sin(\Delta\cdot T+\phi/2)], \tag{A9b}$$

$$\mathcal{C} = 4|C_1|^2|C_2|^2|S_1|^2+2|C_1|^4|S_2|^2+2|S_1|^4|S_2|^2 +4|S_1|^2\left[\mathrm{Re}\left(C_1^2C_2^2\right)\cos(\Delta\cdot T+\phi) + \mathrm{Im}\left(C_1^2C_2^2\right)\sin(\Delta\cdot T+\phi)\right]. \tag{A9c}$$

The output has sinusoidal components in τ with velocity-dependent frequency Δ and amplitude $\mathcal{A}(\Omega, \Delta_{\mathrm{ac}})$, purely constructed from elements of the pulse matrices and thus only dependent on the offset from the light-shifted resonance (with the overall scale determined by the on-resonance Rabi frequency). There is no detuning-dependent phase shift to these harmonic components, though parasitic subharmonics of amplitude $\mathcal{B}(\Omega, \Delta, \Delta_{\mathrm{ac}}, \phi, T)$ become significant at large detunings.

With $\mathcal{A} = \mathcal{C} = 1$, $\mathcal{B} = 0$, and $\delta_{\mathrm{laser}} = 0$, Eq. (A8) resembles the analogous Ramsey output in the integrand of Eq. (4), albeit with an inversion arising from the additional rotation by π. As long as $\mathcal{A} \gg \mathcal{B}$, then, as in Eq. (4), the atomic velocity distribution is well mapped onto the frequency domain, and the scaling by $\mathcal{A}$ can be corrected for by multiplying through by its reciprocal.

The magnitudes of $\mathcal{A}$ and $\mathcal{B}$ are plotted as functions of $\delta_{\mathrm{Doppler}}/\Omega$ in Fig. 8(a), which shows that this criterion is satisfied for $-0.4 < \delta_{\mathrm{Doppler}}/\Omega < 0.4$, where $|\mathcal{B}/\mathcal{A}| < 0.1$. Doppler profiles falling within this window will thus incur little distortion from subharmonics, which would act to artificially narrow broader distributions. As the interferometer time is made longer by increasing T, the oscillations in $\mathcal{B}$ become more rapid but remain within the same envelope.

It should be noted that the velocity distribution will be centered about δ_{laser} in the frequency domain, so the ambiguity

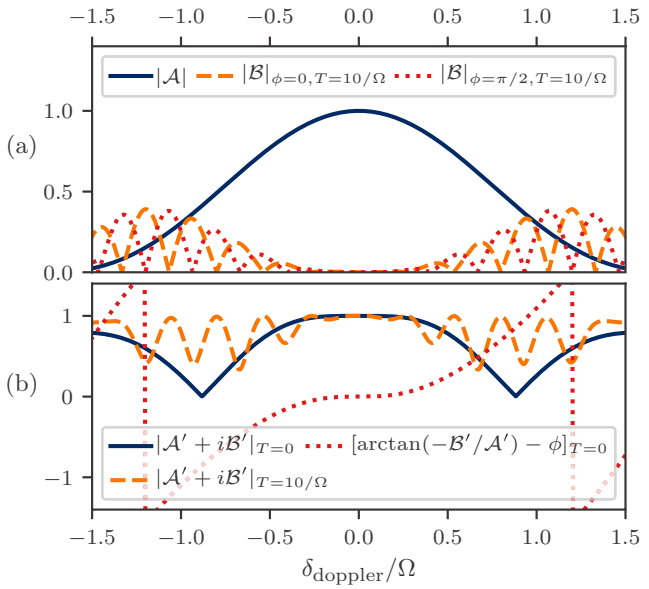

FIG. 8. Amplitudes of frequency components in interferometer outputs as a function of Doppler detuning, in units of the on-resonance Rabi frequency. In these plots, $\delta_{\mathrm{ac}} = \delta_{\mathrm{laser}}$; when this is not the case, the profile is shifted in position by the difference. (a) Amplitudes for $T_1 = T - \tau/2$, $T_2 = T + \tau/2$ interferometer. Solid (blue) line shows amplitude of $\delta_{\mathrm{Doppler}}$ harmonics. Dashed (orange) and dotted (red) lines show the amplitude of $\delta_{\mathrm{Doppler}}/2$ subharmonics with $\phi = 0$ and $\phi = \pi/2$, respectively, when $T = 10/\Omega$. (b) Amplitudes for $T_1 = T$, $T_2 = T + \tau$ interferometer. No subharmonics are present, but the $\delta_{\mathrm{Doppler}}$ harmonics receive a residual detuning-dependent phase shift, plotted as a dotted (red) line for $T = 0$. Solid (blue) line shows the amplitude profile when $T = 0$. Dashed (orange) line shows the profile for $T = 10/\Omega$, demonstrating the appearance of an amplitude modulation in lieu of the presence of subharmonics.

of the dc component $\mathcal{C}(\Omega, \Delta, \Delta_{\mathrm{ac}}, \phi, T)$ can be negated by setting δ_{laser} much larger than the width of the Doppler profile and subtracting it off in analysis.

Equation (A8) can be evaluated as a function of τ and integrated over a distribution of velocities (and hence detunings Δ) to predict the interferometer output for the given velocity distribution. This is shown by the dotted lines in Fig. 9, which are calculated from the distribution measured in Sec. V with the same experimental parameters at $\phi = 0$ and $\phi = \pi/2$.

This analysis assumes completely coherent evolution, no phase or amplitude noise on the laser, and no additional phase terms from external fields. Further, it assumes a perfect two-level atom, as opposed to the ^{85}Rb Raman system with different coupling strengths for magnetic sublevels. Empirically we observe that these factors result in a loss of contrast but do not noticeably affect the shape of the signal, as demonstrated by the solid lines in Fig. 9, which have been vertically centered on the experimental data from Fig. 3 and scaled by a factor of 0.63, demonstrating good agreement. We attribute the slight positive offset of the experimental data to imperfect state preparation or incoherent (single-photon) excitation.

Let us now treat case (b), introduced at the beginning of this appendix as the interferometer in which $T_1 = T$ is kept constant and $T_2 = T + \tau$, in a similar manner. By expanding the trigonometric functions of Eq. (A6), we can isolate the τ

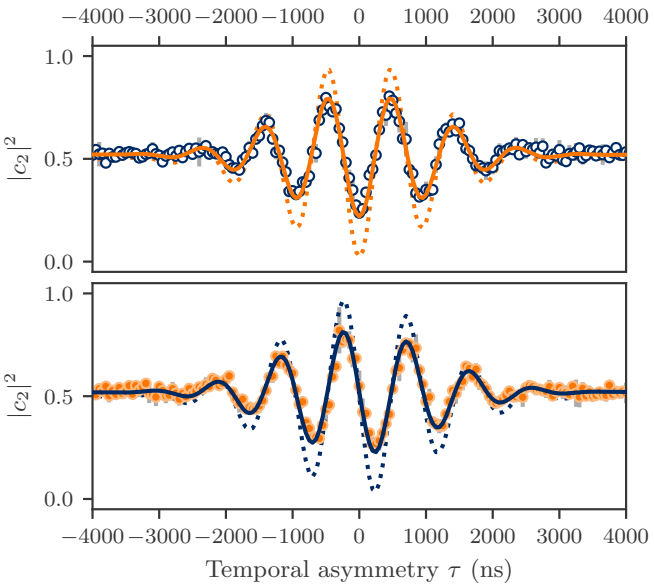

FIG. 9. Empty (blue) and filled (orange) circles, respectively, show the in-phase and quadrature data from Fig. 3. Dashed lines show the output from Eq. (A8) integrated over a 33 μK velocity distribution, as per Fig. 5, with $\delta_{ac} = -2\pi \times 1010$ kHz, $\delta_{laser} = -2\pi \times 1050$ kHz, and $\Omega = 2\pi \times 685$ kHz taken from experimental parameters. Solid lines are the same model vertically centered on the experimental data and scaled by a factor of 0.63. The contrast loss is expected, as the model does not account for sources of dephasing and finite interaction region present in the real experiment, but the shape otherwise agrees well. We attribute the slight vertical offset in the data to incoherent excitation or imperfect state preparation.

dependence into terms of $\sin(\Delta\tau + \phi)$ and $\cos(\Delta\tau + \phi)$ such that the interferometer output can be written in the form

$$|c_2|^2 = \tfrac{1}{2}\{\mathcal{C}' + \mathcal{A}'\cos(\Delta\tau + \phi) + \mathcal{B}'\sin(\Delta\tau + \phi)\}, \quad \text{(A10)}$$

with

$$\begin{aligned}\mathcal{A}' = &-4|C_1|^2|S_2|^2|S_1|^2 \\ &+4|S_1|^2\left[\mathrm{Im}\left(C_1^2C_2^2\right) - |S_1||S_2|\,\mathrm{Im}(C_1C_2)\right]\sin(\Delta\cdot T) \\ &+4|S_1|^2\left[\mathrm{Re}\left(C_1^2C_2^2\right) - |S_1||S_2|\,\mathrm{Re}(C_1C_2)\right]\cos(\Delta\cdot T) \\ &+4|C_1|^2|S_1||S_2|[\mathrm{Im}(C_1C_2)\sin(\Delta\cdot T) \\ &+\mathrm{Re}(C_1C_2)\cos(\Delta\cdot T)], \quad \text{(A11a)}\end{aligned}$$

$$\begin{aligned}\mathcal{B}' = &4[|S_1|^2\,\mathrm{Im}\left(C_1^2C_2^2\right) + (|C_1|^2 - |S_1|^2) \\ &\times|S_1||S_2|\,\mathrm{Im}(C_1C_2)]\cos(\Delta\cdot T) \\ &-4\left[|S_1|^2\,\mathrm{Re}\left(C_1^2C_2^2\right) + (|C_1|^2 - |S_1|^2)\right. \\ &\left.\times|S_1||S_2|\,\mathrm{Re}(C_1C_2)\right]\sin(\Delta\cdot T), \quad \text{(A11b)}\end{aligned}$$

$$\begin{aligned}\mathcal{C}' = &2|C_1|^4|S_2|^2 + 2|S_1|^4|S_2|^2 + 4|C_1|^2|C_2|^2|S_1|^2 \\ &-4|S_1|^3|S_2|[\mathrm{Re}(C_1C_2)\cos(\Delta\cdot T) \\ &+\mathrm{Im}(C_1C_2)\sin(\Delta\cdot T)] \\ &+4|C_1|^2|S_1||S_2|[\mathrm{Re}(C_1C_2)\cos(\Delta\cdot T) \\ &+\mathrm{Im}(C_1C_2)\sin(\Delta\cdot T)]. \quad \text{(A11c)}\end{aligned}$$

Subharmonic components are no longer present in this output, but quadrature terms are, introducing an effective

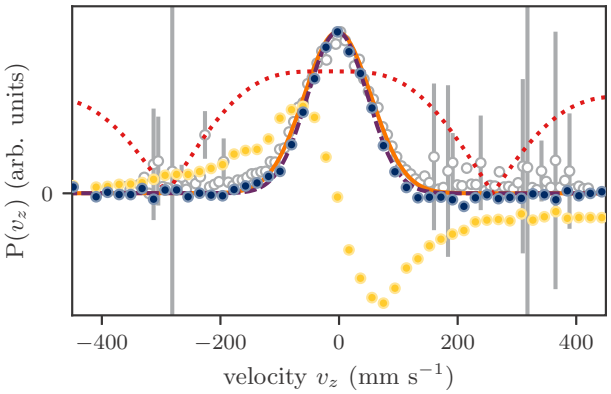

FIG. 10. Interferometric velocimetry measurement with enhanced Ramsey interferometer. Real and imaginary parts of the FFT are shown by dark (blue) and light (yellow) filled circles, respectively, overlaid upon a Doppler spectroscopy profile, empty circles (gray), taken under the same conditions. The real part of the interferometric measurement shows good agreement with the spectroscopic one. The solid (orange) and dashed (purple) lines show Gaussian fits to the spectroscopic and interferometric data, respectively, with corresponding temperatures of 26 and 33 μK. The theoretical amplitude $|\mathcal{A}' + i\mathcal{B}'|$ from Fig. 8(b) is shown as an additional dashed (red) line, plotted from measured experimental parameters.

detuning-dependent phase shift $\arctan(-\mathcal{B}'/\mathcal{A}')$, which, unlike the Ramsey interferometer [27], has a flat gradient through $\Delta_{ac} = 0$. $|\mathcal{A}' + i\mathcal{B}'|$ gives the amplitude of the harmonic components, which, for $T > 0$, exhibits an oscillatory modulation, the envelope of which resembles that of the subharmonics present in case (a).

The case of $T = 0$ warrants special attention. This reduces to a two-pulse $3\pi/2$-$\pi/2$ interferometer, restricting the pulse separation to $\tau > 0$. This can still yield good velocimetry results when the gradient of the detuning-dependent phase shift is small, as it is about $\Delta_{ac} = 0$, unlike in a Ramsey interferometer [27]. This case is considered in Appendix B.

APPENDIX B: ENHANCED RAMSEY INTERFEROMETER

In a two-pulse interferometer, data collection is inherently restricted to the $\tau > 0$ window, mathematically expressed by multiplying the time domain output by the Heaviside step function $\Theta(\tau)$. In the frequency (velocity) domain, this manifests as a convolution with the Fourier transform of the step function,

$$\tilde{\Theta}(\omega) = \frac{i}{\sqrt{2\pi}\omega} + \sqrt{\frac{\pi}{2}}\delta(\omega), \quad \text{(B1)}$$

$\delta(\omega)$ being the Dirac delta function. This introduced an imaginary component to the output, but it leaves the velocity distribution unaltered in the real part.

In a realistic Ramsey interferometer [Fig. 1(b)] where the pulses are of finite length, setting the separation to $\tau = 0$ is not equivalent to setting the effective interferometer period to 0. The result of this is a multiplication by $\Theta(\tau - \delta\tau)$, where $\delta\tau$ is an offset determined by the length of the pulses. This introduces a phase factor into the first term of Eq. (B1),

irreversibly mixing the real part of the $\delta\tau = 0$ output with the imaginary part so that the velocity distribution is irretrievable from a single measurement [27].

As touched upon at the end of Appendix A, the asymmetric Mach-Zehnder interferometer case (b) with $T = 0$ is a two-pulse $3\pi/2$-$\pi/2$ interferometer. This has the properties of a Ramsey-type interferometer, but with a degree of cancellation of the phase picked up during the pulses. While the Ramsey interferometer has a linear dependence of the phase shift on detuning, equivalent to an offset of the effective time origin, for the $3\pi/2$-$\pi/2$ interferometer the lowest order term in the phase shift is cubic. This gives it a flat gradient about zero detuning, a property shared by the shift in amplitude [Fig. 8(b)].

Preliminary results, shown in Fig. 10, show that the real parts of the Fourier transformed interferometer provide an effective measure of the velocity profile. Distortion due to the time domain truncation is primarily restricted to the imaginary parts. The detuning-dependent amplitude from Fig. 8(b), plotted from measured experimental parameters, is shown as a red (dotted) line, though the data have not been corrected by multiplying by its reciprocal. The reduction in amplitude is $<10\%$ across two standard deviations (95%) of the Gaussian distribution fitted to the real data, which are negligibly affected by correction (although the imaginary data are distorted). This broad, flat, profile offers a potential advantage of what we term the enhanced Ramsey method.

The measurement is overlaid upon a spectroscopic measurement taken under the same conditions and they are in good agreement, with the interferometric measurement appearing slightly narrower. We can attribute this discrepancy to artefacts of the Doppler spectroscopy discussed in Sec. VI and sensitivity of the interferometric measurement to pulse rise-time at small τ.

[1] M. Hohmann, F. Kindermann, T. Lausch, D. Mayer, F. Schmidt, and A. Widera, Phys. Rev. A **93**, 043607 (2016).

[2] J. Millen and A. Xuereb, New J. Phys. **18**, 011002 (2016).

[3] P. D. Lett, R. N. Watts, C. I. Westbrook, W. D. Phillips, P. L. Gould, and H. J. Metcalf, Phys. Rev. Lett. **61**, 169 (1988).

[4] M. Kasevich, D. S. Weiss, E. Riis, K. Moler, S. Kasapi, and S. Chu, Phys. Rev. Lett. **66**, 2297 (1991).

[5] I. G. Hughes, J. Mod. Opt. **65**, 640 (2018).

[6] J. Stenger, S. Inouye, A. P. Chikkatur, D. M. Stamper-Kurn, D. E. Pritchard, and W. Ketterle, Phys. Rev. Lett. **82**, 4569 (1999).

[7] B. Deh, C. Marzok, S. Slama, C. Zimmermann, and P. W. Courteille, Appl. Phys. B **97**, 387 (2009).

[8] D.-S. Lü, Q.-Z. Qu, B. Wang, J.-B. Zhao, L. Liu, and Y.-Z. Wang, Chin. Phys. Lett. **28**, 063201 (2011).

[9] P. Zhang, Y. Guo, Z. Li, Y.-c. Zhang, Y. Zhang, J. Du, G. Li, J. Wang, and T. Zhang, J. Opt. Soc. Am. B **28**, 667 (2011).

[10] S. Pradhan and B. N. Jagatap, Rev. Sci. Instrum. **79**, 013101 (2008).

[11] T. M. Brzozowski, M. Maczynska, M. Zawada, J. Zachorowski, and W. Gawlik, J. Opt. B **4**, 62 (2002).

[12] P. D. Featonby, G. S. Summy, C. L. Webb, R. M. Godun, M. K. Oberthaler, A. C. Wilson, C. J. Foot, and K. Burnett, Phys. Rev. Lett. **81**, 495 (1998).

[13] B. Saubaméa, T. W. Hijmans, S. Kulin, E. Rasel, E. Peik, M. Leduc, and C. Cohen-Tannoudji, Phys. Rev. Lett. **79**, 3146 (1997).

[14] E. Maréchal, R. Long, T. Miossec, J.-L. Bossennec, R. Barbé, J.-C. Keller, and O. Gorceix, Phys. Rev. A **62**, 053603 (2000).

[15] S. Riedl, G. W. Hoth, B. Pelle, J. Kitching, and E. A. Donley, J. Phys.: Conf. Ser. **723**, 012058 (2016).

[16] A. Peters, K. Y. Chung, and S. Chu, Metrologia **38**, 25 (2001).

[17] T. L. Gustavson, A. Landragin, and M. A. Kasevich, Class. Quantum Grav. **17**, 2385 (2000).

[18] M. Kasevich and S. Chu, Phys. Rev. Lett. **67**, 181 (1991).

[19] B. Barrett, A. Bertoldi, and P. Bouyer, Phys. Scr. **91**, 053006 (2016).

[20] G. D'Amico, L. Cacciapuoti, M. Jain, S. Zhan, and G. Rosi, arXiv:1803.11492.

[21] C. J. Bordé, Phys. Lett. A **140**, 10 (1989).

[22] N. F. Ramsey, Phys. Rev. **78**, 695 (1950).

[23] K. Bongs, R. Launay, and M. Kasevich, Appl. Phys. B **84**, 599 (2006).

[24] P. R. Berman, *Atom Interferometry* (Elsevier Science, Amsterdam, 1996).

[25] A. A. Michelson, London, Edinburgh, Dublin Philos. Mag. J. Sci. **31**, 338 (1891).

[26] R. Bell, *Introductory Fourier Transform Spectroscopy* (Academic Press, New York and London, 1972).

[27] M. Carey, M. Belal, M. Himsworth, J. Bateman, and T. Freegarde, J. Mod. Opt. **65**, 657 (2018).

[28] In practice, the time series data are unavoidably truncated, and the time origin determines how the velocity distribution is divided between the real and imaginary parts of the transform, but the absolute value always offers a good measure.

[29] A. Dunning, R. Gregory, J. Bateman, N. Cooper, M. Himsworth, J. A. Jones, and T. Freegarde, Phys. Rev. A **90**, 033608 (2014).

[30] P. Gillot, B. Cheng, S. Merlet, and F. Pereira Dos Santos, Phys. Rev. A **93**, 013609 (2016).

[31] A. Dunning, R. Gregory, J. Bateman, M. Himsworth, and T. Freegarde, Phys. Rev. Lett. **115**, 073004 (2015).

[32] The stochastic optical pumping process from the $|5S_{1/2}, F = 3\rangle$ to $|5S_{1/2}, F = 2\rangle$ state via the MOT cooling beam has a $1/e$ time constant on the order of 100 μs, depending on the detuning and power of the cooling beam that are tweaked to control the atomic temperature. The transfer from the $|5S_{1/2}, F = 2\rangle$ to $|5S_{1/2}, F = 3\rangle$ state via the resonant repump beam is faster by an order of magnitude. Imperfect state preparation causes a loss of fringe visibility without affecting the form of the signal.

[33] N. Cooper, J. Woods, J. Bateman, A. Dunning, and T. Freegarde, Appl. Opt. **52**, 5713 (2013).

[34] A. Dunning, Ph.D. thesis, University of Southampton, 2014, https://eprints.soton.ac.uk/364735.

[35] C. G. Townsend, N. H. Edwards, C. J. Cooper, K. P. Zetie, C. J. Foot, A. M. Steane, P. Szriftgiser, H. Perrin, and J. Dalibard, Phys. Rev. A **52**, 1423 (1995).

[36] L. P. Parazzoli, A. M. Hankin, and G. W. Biedermann, Phys. Rev. Lett. **109**, 230401 (2012).

[37] M. H. Anderson, J. R. Ensher, M. R. Matthews, C. E. Wieman, and E. A. Cornell, Science (New York, N.Y.) **269**, 198 (1995).

[38] G. Afek, J. Coslovsky, A. Courvoisier, O. Livneh, and N. Davidson, Phys. Rev. Lett. **119**, 060602 (2017).

[39] I. I. Rabi, N. F. Ramsey, and J. Schwinger, Rev. Mod. Phys. **26**, 167 (1954).

[40] R. P. Feynman, F. L. Vernon, and R. W. Hellwarth, J. Appl. Phys. **28**, 49 (1957).

[41] R. Stoner, D. Butts, J. Kinast, and B. Timmons, J. Opt. Soc. Am. B **28**, 2418 (2011).

[42] http://doi.org/10.5258/SOTON/D0383.

Correction: One of the previously listed co-authors, David Elcock, requested that his name be removed from the author list, which has been implemented. A statement of thanks to Dr. Elcock has been added to the Acknowledgments.